Advanced Materials Design Group amdg.science

Sodium mechanics: effects of temperature, strain rate, and grain rotation and implications for sodium metal batteries

LePage W, Chen Y, Poli A, Thouless MD, Dasgupta NP

PUBLISHED AS

LePage W, Chen Y, Poli A, Thouless MD, Dasgupta NP. "Sodium mechanics: effects of temperature, strain rate, and grain rotation and implications for sodium metal batteries." Extreme Mechanics Letters 52, 101644 (2022).

https://doi.org/10.1016/j.eml.2022.101644

This is the accepted manuscript of an article published by Elsevier. The Version of Record is available at https://doi.org/10.1016/j.eml.2022.101644.

LICENCE

This manuscript version is made available under the CC-BY-NC-ND 4.0 license (https://creativecommons.org/licenses/by-nc-nd/4.0/).

Self-archived by the authors in accordance with the publisher's self-archiving policy. Provided for educational and personal use. Please cite the version of record.

ACCEPTED MANUSCRIPT · SELF-ARCHIVED AUTHOR VERSION

Sodium mechanics: effects of temperature, strain rate, and grain rotation and implications for sodium metal batteries

William S. LePage[1,2], Yuxin Chen[1], Andrea Poli[1], M. D. Thouless[1,3], and Neil P. Dasgupta[1,3†]

[1]Department of Mechanical Engineering, University of Michigan, Ann Arbor, MI, 48109, USA
[2]Present address: Department of Mechanical Engineering, University of Tulsa, Tulsa, OK, 74104, USA
[3]Department of Materials Science and Engineering, University of Michigan, Ann Arbor, MI, 48109, USA
[†]Correspondence: ndasgupt@umich.edu

Abstract

Sodium-metal batteries are an attractive energy storage technology, owing to the low cost and relative earth abundance of sodium. However, despite the importance of electro-chemo-mechanical phenomena in alkali-metal batteries, experiments on the mechanical properties of metallic Na are relatively scarce, especially in terms of its viscoplastic response. In this work, we measured the temperature- and rate-dependent deformation of sodium by performing tensile tests in inert gas environments. Digital image correlation measurements were performed to track the local strain and rotation fields. Temperature-dependent experiments were used to experimentally calibrate the activation energy for creep. Furthermore, local deformation measurements of sodium suggest that grain-size and crystallographic orientation effects may be important considerations for sodium-based batteries. Finally, the implications of creep on the performance of Na-metal batteries discussed, providing guidance for future modeling efforts.

Keywords: sodium, mechanical properties, batteries, creep

1 Introduction

As the production of lithium-based batteries escalates, concerns have been raised about the stability of supply chains for battery materials, especially cobalt[1] and lithium (Li).[2] To increase supply chain stability, sodium (Na) is an attraction option to supplement Li-based batteries.[3] While Na is almost twice as dense (0.97 g/cc) as Li (0.53 g/cc), it is about 1,000 times more abundant in Earth's crust,[4] as outlined in Table S1. Furthermore, Na-based batteries are compatible with cobalt-free cathodes and current collectors made of aluminum (which is more easily sourced than the copper foils currently used with Li).[5]

Na-based batteries take diverse forms, including Na-ion batteries (NIBs) that are analogous to Li-ion batteries (LIBs),[6–10] Na-O_2 batteries,[11], aqueous Na batteries,[12,13], and solid-state Na-metal batteries.[14] For both Li and Na solid-state batteries, early investigations using Na-metal anodes were instrumental in the development of effective solid-state electrolytes. Specifically, there is a long history of literature on the degradation mechanisms of Na-β''-alumina solid electrolytes, with two distinct failure modes: rapid propagation of Na-filled cracks (Mode I), and slow

degradation and internal deposition of Na resulting from chemical changes in the electrolyte (Mode II).[15,16] Present work continues to advance the state of the art for both Li and Na solid-state electrolytes in a synergistic way.

To advance Na-based batteries, a thorough understanding of the mechanical properties of Na is important. However, experiments on the mechanical properties of Na are relatively scarce. A number of studies have focused on the elastic properties of Na,[17–20] while few have characterized the viscoplastic properties of Na, especially at temperatures at or above room temperature. Since Na has a low melting point (98°C) and homologous temperature (0.8 at 25°C), which is even lower than that of Li (Table S1), creep is expected to play a significant role in Na deformation at temperatures and strain rates that are relevant to Na batteries, as has been demonstrated in prior work on Li.[21,22]

Early works on the viscoplasticity of Na focused on its anomalous deformation mechanisms at cryogenic temperatures.[23–25] Hull and Rosenberg reported the stress-strain responses of Na in tension from 4.2 to 195 K at a strain rate of approximately 1×10^{-4} s^{-1}.[23] Also, Herke, Kirchner, and Schoeck characterized the plastic behavior of single-crystal Na.[24] The critical resolved shear stress was observed to be orientation-dependent for temperatures below 150 K. Measurements above 300 K were said to be conducted, but quantified results above 300 K were not reported.[24]

For the viscoplasticity of Na, power-law creep is a dominant deformation mechanism, and three prior works[26–28] have measured the power-law creep exponent of Na at room temperature. Sargent and Ashby[26] characterized Na in compression at 293 K for strain rates between 1×10^{-6} and 5×10^{-4} s^{-1} and proposed a power-law creep model. The strain rate ($\dot{\varepsilon}$) for power-law creep can be expressed as a function of creep stress (σ_{creep}) and temperature (T),[21] with

$$\dot{\varepsilon} = A_c \left(\sigma_{\text{creep}}\right)^m \exp\left(\frac{-Q_c}{\bar{R}T}\right) \tag{1}$$

for creep constant A_c, power-law exponent m, activation energy Q_c, and molar gas constant $\bar{R}$ = 8.31 J mol^{-1} K^{-1}. Sargent and Ashby calibrated the power-law exponent from their compression experiments at 293 K.

Recently, Fincher et al.[27] and Wang et al.[28] investigated the elastic, plastic, and creep responses of bulk Na at room temperature. The study from Fincher et al.[27] spanned several time and length scales through an experimental suite of

nanoindentation, microindentation, and bulk compression. As with prior work on Li,[29–33] the strength of Na was shown to increase at the nanoscale, as corroborated by recent *in situ* observations via environmental transmission electron microscopy.[34] From Fincher et al.,[27] the strain-rate sensitivity exponent n (the inverse of power-law creep exponent m) was determined to be $n = 0.14$ ($m = 7.1$) from nanoindentation and $n = 0.20$ ($m = 5.0$) from bulk compression. The study from Wang et al.[28] included the first measurements of the shear modulus and Poisson's ratio of Na. It was hypothesized that the lower creep exponent for Na ($m = 5$)[27,28] compared to that of Li ($m \approx 6.5$)[21,35] may indicate that creep in Na is driven primarily by lattice diffusion. Therefore, it was postulated by Wang et al.[28] that the activation energy for Na creep could be close to the activation energy for Na lattice diffusion ($Q = 44$ kJ mol^{-1} [36,37]). However, to date, the temperature dependence of power-law creep in Na has not been experimentally measured.

To develop a complete power-law creep model of Na, experiments that span a wide range of temperatures are needed. To address this knowledge gap, the goal of this work is to measure and understand the temperature- and strain-rate-dependent deformation of Na. Herein, measurements of bulk Na samples in tension are presented over a range of temperatures (273 to 348 K) and strain rates (4×10^{-4} and 3×10^{-3} s^{-1}). These measurements enable a calibration of the activation energy for power-law creep of Na. Compared to prior works that have characterized the viscoplastic deformation of Na (Table S2),[26–28] this work is the first to present local deformation and rotation measurements (via digital image correlation, or DIC). Finally, we discuss the relevance of the temperature- and rate-dependent properties of Na in the context of Na-based batteries.

2 Material and methods

The present work uses many of the same experimental techniques as our previous work on Li,[21] which were developed to address the difficulties of experimentation on alkali metal systems in inert environments, and have to be adapted according to the material system. In particular, new aspects of the current study from an experimental perspective include the need to prepare thin samples of Na from the commercially available forms, and the need for different DIC patterning techniques.

2.1 Sample preparation

Samples for analysis were prepared in an inert Ar glovebox environment from large pieces of elemental Na ($\geq$ 99.8% metals basis, shipped in kerosene; Sigma-Aldrich). As high-purity Na foils are not commercially available, this work required producing the foils manually (unlike our prior work on Li).[21] First, clean pieces of Na were produced by using a razor blade to cut away the native oxide layer of the as-received Na. Next, the clean pieces of Na were melted on a sheet of aluminum foil on a hot plate to produce a sheet geometry. After melting, the sheets of Na were allowed to cool on the hot plate. The as-melted sheet thickness was approximately 10 mm. After melting and cooling, and prior to rolling, the grain sizes were measured to be 1.03 ± 0.60 mm (Figure S1), using a digital optical microscope (Keyence VHX-7000).

After the Na pieces were cleaned, melted, and cooled, they were placed between two polyether ether ketone (PEEK) polymer films and rolled into flat sheets. After each rolling pass, the direction of rolling was alternated in the plane of the sheet. In this way, there were many different rolling directions for each Na sheet, such that in-plane anisotropy is likely to be minimized. However, as described in Section 3.1, the rolled sheets likely had differences in the grain orientations between the in-plane and through-thickness directions, which could have caused more deformation in the through-thickness direction and less deformation in the in-plane directions. Two thicknesses of samples were produced. The majority of samples were rolled to a thickness of 5 mm and were cut with 5 mm wide cross sections. An additional, thinner set of samples were rolled to a thickness of 3 mm and were cut with 3 mm wide cross sections. In these narrower samples, only a few grains were present for a given cross-sectional area for the 3×3 mm samples, and there was significant grain rotation, as described in Section 3.3. For all experiments used to calibrate the power-law creep model, the larger samples (with 5×5 mm cross sections) were used. The grain size did not measurably change after rolling to 3 mm or 5 mm, nor after mechanical testing at 298 K and 348 K (Figure S1). Furthermore, no significant difference was found in the optical micrographs of the cross-sections and the probability and cumulative distributions of the various samples conditions (Figure S2).

2.2 Methods for strain-rate dependent deformation

The strain-rate dependent deformation of Na was characterized with a custom, glovebox-incorporated mechanical testing system that was introduced in prior work.[21] The setup

consisted of a stereo digital image correlation (DIC) setup and a custom load frame in an Ar glovebox. The system used a screw-driven actuator (Newport TRB25CC) for constant-displacement-rate measurements. Force was measured with a load cell (Futek LSB200, 2.2 N capacity). For 3-D DIC measurements, two machine vision cameras were mounted on a tripod outside of the Ar glovebox, as shown in Figure S3. Cross polarization was used to improve the DIC measurements.[38] Further details about the DIC setup are provided in Table S3.

Tensile samples were cut from Na foil with razor blades in a custom jig, following the method of prior work.[21] For DIC measurements, a speckle pattern was applied to each sample. For all samples used in the calibration of the power-law creep model, with 5×5 mm cross-sections, the pattern consisted of MgO powder (Frey Scientific) and polyethylene microspheres (212 to 250 µm diameter, Cospheric). This sequence of dark-on-light speckles improves DIC results by increasing contrast.[39] For the speckle pattern in smaller samples, with 3×3 mm cross-sections, graphite was used, following the procedure from prior work.[21] While the graphite patterning method was well suited to the smaller Li samples in our prior work, the larger Na samples in this work required larger speckles in the pattern, so the diameter of polyethylene microspheres was selected accordingly (with at least 3 pixels per speckle.[40] While the sodium deforms, each microsphere itself does not appreciably deform, but this lack of deformation in speckle features has negligible influence on the quality of DIC measurements.[41] To produce the speckle patterns with microspheres, the Na samples were first submerged in MgO and gently agitated to promote adhesion with the sample surface. Next, a partial coating of polyethylene microspheres was applied by sprinkling them over the samples.

The DIC analyses were performed with Vic3D 7 (Correlated Solutions, Inc.). The stereo camera system was calibrated with the calibration grid inside the glovebox, and the cameras were not disturbed between calibration and the conclusion of the experiment. Further details about the DIC software parameters are provided in Table S3. Finite Lagrangian in-pane strains (ε_{xx}, ε_{xy}, and ε_{yy}) were computed from spatial derivatives of the displacements, and the differentiation used a Gaussian-weighted filter with a size of 15×15 DIC data points. In-plane rotations were also computed with a Gaussian-weighted filter with a size of 15×15 DIC data points. For each sample, the axial strain (ε_{YY}) was measured from the average of a selected area of the DIC data. The selected area was centered over the region in the gauge section with

the largest axial strain, and the height of the selected area was reduced until convergence was found (at a height of 2 mm) such that further reduction in its height did not change the average strain value in the selected area.[21] True strain ($\varepsilon_{\text{true}}$) was computed from $\varepsilon_{\text{true}} = \ln(1+\varepsilon_{\text{YY}})$, assuming that the deformation was volume-preserving. True stress (σ_{true}) was computed as $\sigma_{\text{true}} = \sigma_{\text{nom}}(1+\varepsilon_{\text{nom}})$. We note that the strain rate from sample to sample could not be precisely duplicated by the instrumentation: while the global grip displacement rate could be prescribed, the local strain rate in the gauge section could not be directly controlled. Therefore, strain rate is a value that was measured for each sample, and only one test is presented for each strain rate.

2.3 Methods for temperature dependent deformation

The deformation of Na with respect to temperature was measured using a dynamic mechanical analyzer (DMA) equipped with an environmental chamber (TA Instruments RSA-G2). Experiments were conducted between 273 K and 348 K in inert gas environments. For the cooled experiments at 273 K, the inert gas in the environmental chamber was N_2 gas from a liquid N_2 source. For the heated experiments at 298, 323, and 348 K, the inert gas in the environmental chamber was Ar gas. Tensile samples with straight sides were cut from Na foil with a razor blade. The samples tested had thicknesses of 5.03 ± 0.30 mm and widths of 5.06 ± 0.12 mm, as measured by calipers. Along with the force reading (P) from the DMA, the thickness and width of each sample was used to calculate its cross-sectional area (A) and nominal stress ($\sigma_{\text{nom}} = P/A$). At ambient temperature and with a brief exposure (< 1 min) to atmosphere, the samples were clamped in the DMA. This brief air exposure resulted in slight oxidation of the Na surface. From postmortem examination of the sample cross-section in an optical microscope (Figure S4), the layer of oxidation was 25 μm, or 1% of the cross-sectional area. The gauge length of the samples was 15 mm. True strains ($\varepsilon_{\text{true}}$) were computed from the grip strain ($\varepsilon_{\text{grip}}$), following $\varepsilon_{\text{true}} = \ln\left(1+\varepsilon_{\text{grip}}\right)$. The strain range was restricted to less than 2.5% in the DMA experiments. True stresses (σ_{true}) were computed by assuming that deformation was volume-preserving, following $\sigma_{\text{true}} = \sigma_{\text{nom}}\left(1+\varepsilon_{\text{grip}}\right)$. From ambient temperature, the samples were cooled or heated to the experiment temperature under constant force control, as described in prior work.[21] This maintained a stress of approximately 0 MPa while the sample and setup expanded or contracted during heating or cooling, respectively.

The combination of DMA and DIC techniques were essential for this work. DIC

provided information about local sample deformation, but our glovebox-integrated DIC platform did not allow for heating or cooling of the sample, which was only feasible in the DMA. The DMA results measured strain from the grip displacements, providing an average strain measure for the full sample length. On the other hand, the DIC results used strain measured from the central gauge section. While DIC may have a larger error for very small strains («1%, as small errors from image noise, camera calibration inconsistencies, etc. have a higher relative contribution for very small strain measurements), DIC is more suitable for measuring large strains (>1%), because the DMA grip strains only provide a global average and do not capture strain localization in the gauge section. Since DIC provides more accurate strain measurements over a larger range of strains and the DMA had a narrower range of possible strain rates, the results from DIC were used to calibrate the power-law exponent.

3 Results

3.1 Results of strain-rate dependent deformation

Strain maps from DIC were measured from tensile tests of six samples with 5×5 mm cross sections at different displacement rates. Figure 1 presents the axial and in-plane rotation maps for the sample at 4×10^{-4} s^{-1}. The local strain and rotation fields of this sample, as described below, were representative of the other five samples. Axial strain localized in the central region of the sample, where the cross-sectional area is minimum, similar to prior work on Li.[21] The magnitude of in-plane shear strain remained nearly zero throughout the tests (Figure S5), which confirms that the principal strains are aligned in the X and Y principal directions.

From the in-plane rotation field, the portions of the sample above and below the central region had a small degree of relative rotation (less than 3°). There was a minor amount of rotation in the upper portion of the sample, with the central region acting as a hinge. This is in contrast with the inhomogeneous, local rotations found in the set of samples with smaller dimensions (with only 3×3 mm cross sections), as described in Section 3.3. Given the minor degree of in-plane shear and in-plane rotation in the six samples with 5×5 mm cross sections, there was minimal deviation from uniaxial behavior. Thus, the 5×5 mm samples were suitable for measurements to calibrate power-law creep and were used in the analysis below.

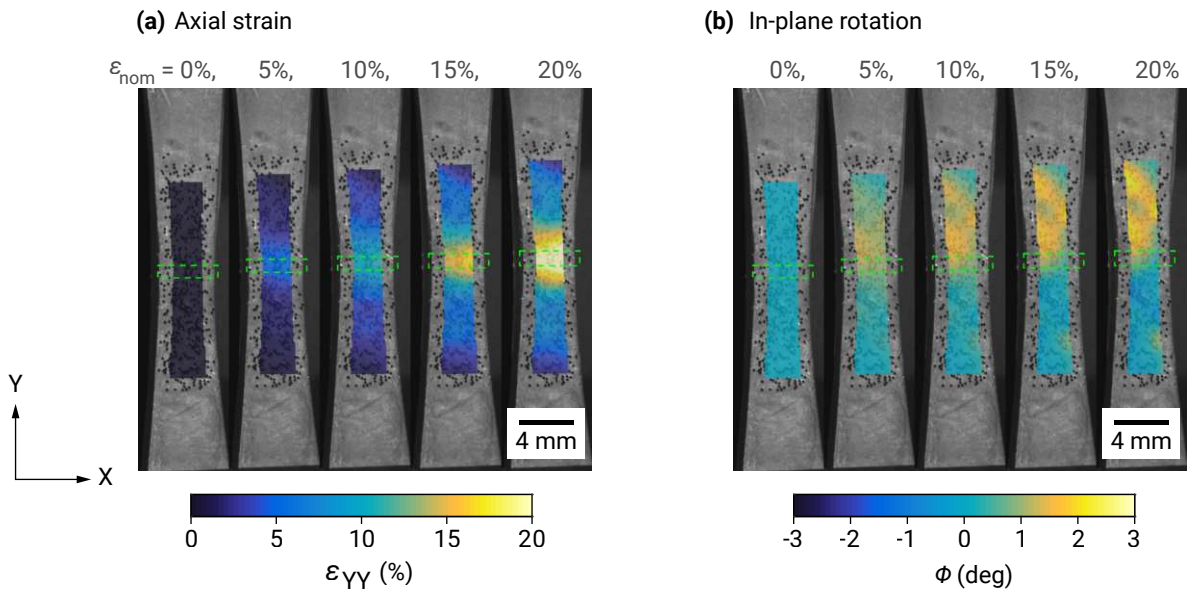

Figure 1: DIC fields of axial strain (ε_{YY}) and in-plane rotation (ϕ) for a representative sample with 5×5 mm cross sections at 4×10^{-4} s^{-1} nominal strain rate. The selected area for ε_{nom} is shown in the central boxes with dashed lines. The in-plane shear fields are also shown in Figure S5.

Consistent with previous measurements,[26–28] the stress-strain response of Na was strongly dependent on strain rate. Tensile experiments were conducted with true strain rates between 4×10^{-4} and 3×10^{-3} s^{-1} (Figure 2). Average strain rates were calculated within the range of ε_{true} between 2% and 10% (Figure 2b). For all of the strain rates tested, viscoplastic flow at a nearly constant stress value was observed before approximately 2% strain.

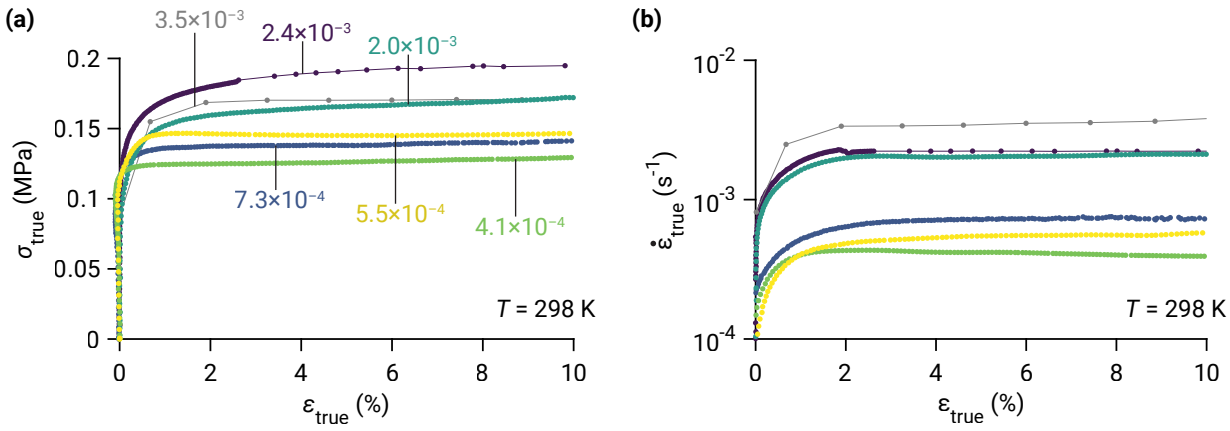

Figure 2: (a) Stress-strain responses of Na at 298 K at various strain rates, measured with DIC. (b) Strain-rates with respect to strain for the same samples shown in the stress-strain curves. Owing to frame rate limitations of the DIC cameras, the sample rate appears sparse in the two fastest strain rates (with connecting lines between points to aid visualization).

While the rate-dependent responses from Figure 2(a) show small variations when viewed in stress-strain space, the overall trend can be clearly seen in Figure 3. Using the average values of true stress and true strain rate for each sample for the true strain values between 2 and 10% strain, the power-law exponent was fitted as $m = 5.6$. This value of the power-law exponent is consistent with prior work,[26–28] as illustrated in Figure S9.

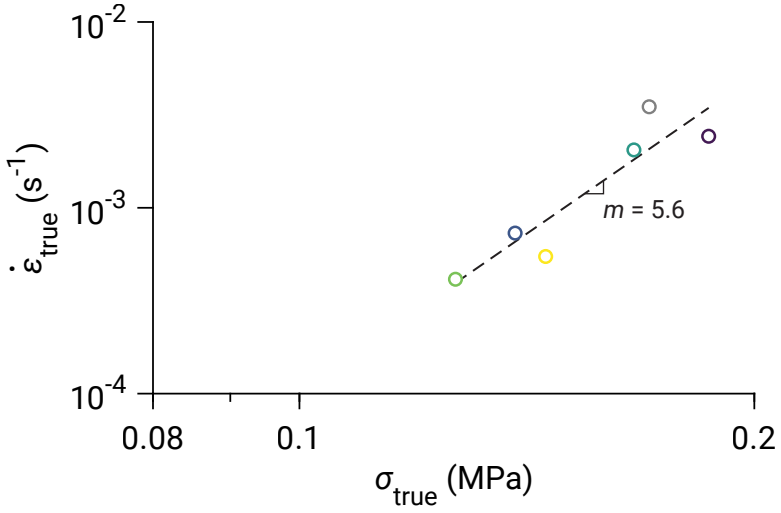

Figure 3: The average values of true stress and true strain rate from DIC are shown from each experiment presented in Figure 2. The fitted slope to these points is m.

Owing to anisotropic contraction in the sample thickness direction, the experiments deviated from Levy-Mises flow in the front plane of the sample (Figure 4). It is hypothesized that the additional contraction in the thickness was due to the crystallographic texture of the large grains, because volume is necessarily preserved during plastic deformation. Specifically, differences in grain orientation between the in-plane and through-thickness directions could have caused more deformation in the through-thickness direction (ε_{ZZ}) and less deformation in the transverse direction (ε_{XX}), while still maintaining volume-preserving plasticity. The larger relative deformation in the through-thickness direction is consistent with recent observations on other rolled alkali metals, including Li.[42] In the present work, the tensile samples were always prepared with the plane of the axial (ε_{XX}) and transverse (ε_{YY}) directions in the plane of the rolled sodium. Therefore, the observed anisotropy is consistent with the expected texture in the sample from rolling.

To further validate this anisotropic deformation in the Na samples used here, postmortem optical microscopy was performed (Figure S6). Three-dimensional topological maps of the sample using focus variation microscopy[43] showed preferential slip plane formation in the through-plane direction compared to the in-plane direction. This indicates anisotropy in the samples that increased the relative amount of deformation in the through-plane direction compared to the in-plane direction, which could be responsible for the deviation from Levy-Mises flow observed in the front plane of the samples.

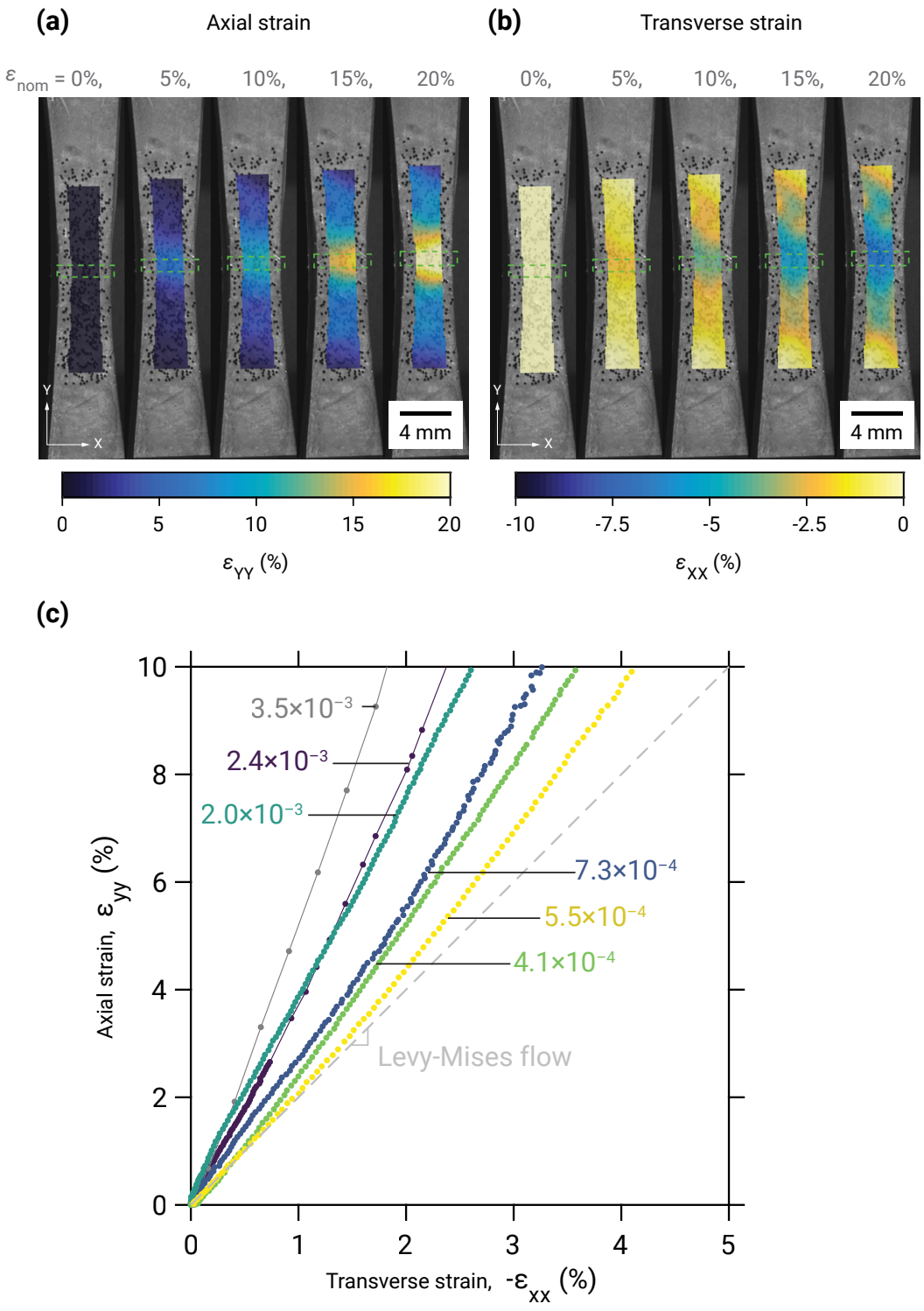

Figure 4: (a) Axial strain fields and (b) transverse strain fields from the same sample plotted in Figure 1 (at a true strain rate of 4.1×10^{-4} s^{-1}). (c) The average axial strains (ε_{YY}) and transverse strains (ε_{XX}) within the inspected area for each experiment. Levy-Mises flow would be observed when the transverse strains are negative one-half of the axial strains, as indicated by the dashed line.

3.2 Results of temperature dependent deformation

Tensile tests were conducted between 273 and 348 K at a nominal strain rate of 5×10^{-4} s^{-1} (Figure 5). In agreement with power-law creep behavior, the stress-strain response of Na was strongly dependent on temperature. At all temperatures from 273 to 348 K, the responses were dominated by viscoplastic flow. As shown in Figure S8, the measurements at 298 K with the DMA were consistent with those from the DIC measurements in Figures 1–3. Specifically, for the DIC measurement, the flow stress was 0.146 MPa, and for the DMA measurement, the flow stress was 0.142 MPa in the first sample and 0.149 MPa in the second.

To calibrate the activation energy for power-law creep (Q_c), the average stress values between 0.5% and 2.5% true strain were fitted to an Arrhenius relationship, yielding $Q_c = 40 \pm 4$ kJ mol^{-1}. This is consistent with a value of $Q_c = 42$ to 43 kJ mol^{-1}, which has been reported for sodium lattice diffusion.[36,37,44] We note that the fitted of Q_C will be influenced by the uncertainty in the power-law exponent (m), which has been measured as 4.2,[26] 5.0,[27,28], and 5.6 (present work).

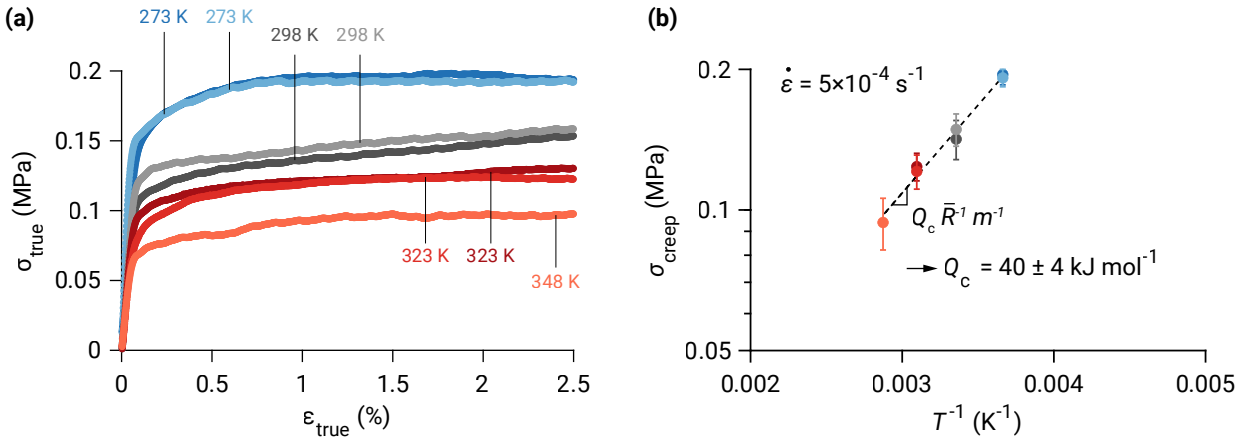

Figure 5: (a) The mechanical response of Na at $5{\times}10^{-4}$ s^{-1} with respect to temperature, from measurements in the DMA. (b) The activation energy for creep (Q_c) was calibrated from the slope between inverse temperature and the average stress values corresponding to true strains between 0.5% and 2.5%, from (a). The error bars at each temperature indicate the range of the stress over this strain range. The error range in Q_c is the 95% confidence interval for the corresponding t-distribution.

With the strain-rate-dependent data from Figure 3 and the temperature-dependent data from Figure 5, the power-law creep parameters for Equation (1) were calibrated. The

material parameters for the model are summarized in Table 1.

m	Q_c (kJ mol^{-1})	$A_c^{-1/m}$ ((s^{-1} Pa^{-m})$^{-1/m}$)
5.6	40	3.1×10^4

Table 1: The power-law creep exponent (m), activation energy (Q_c), and creep constant (A_c) from Equation (1) were calibrated with the experiments at different strain rates (Figure 3 and temperatures (Figure 5).

3.3 Observation of grain rotation

For samples produced with smaller cross-sectional areas (3×3 mm cross-sections), deformation was not uniform through the gauge section and did not localize in a consistent way (unlike the samples with 5×5 mm cross-sections, which were used exclusively in the measurements to calibrate the power-law creep model). For an experiment at 1×10^{-3} s^{-1}, the DIC fields are shown in Figure 6 for the axial strain and in-plane rotation. The in-plane rotation appeared in distinct regions with about 1 mm diameters. Within each distinct region, the angle of rotation was approximately constant, while neighboring regions could differ by ±3° (Figure 6c).

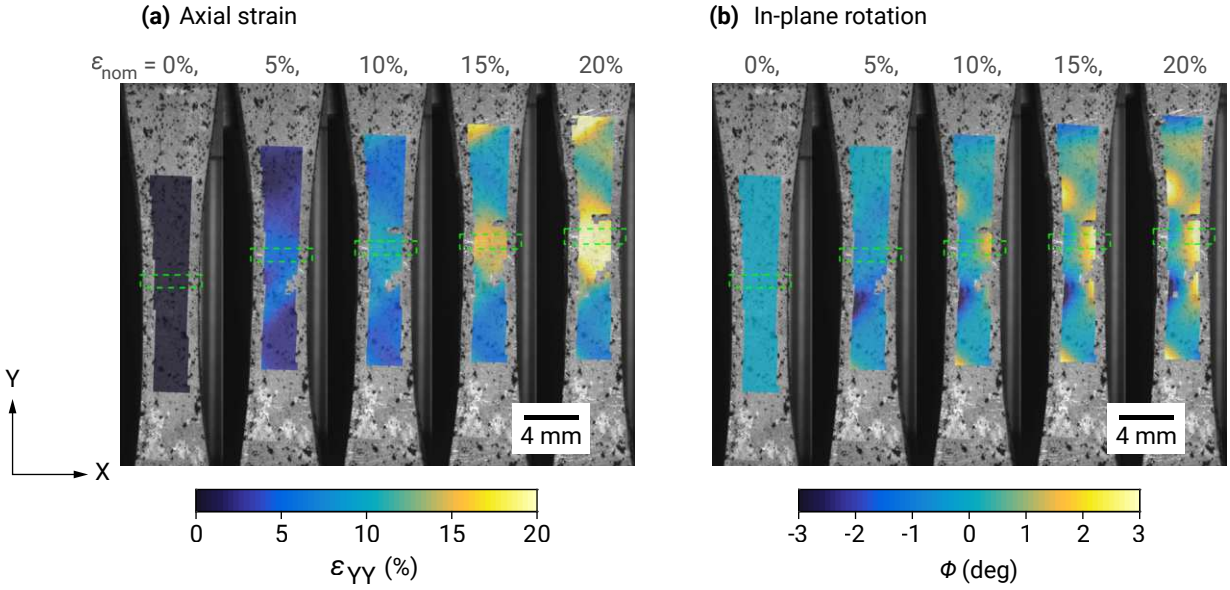

Figure 6: Grain rotation was prevalent for the smaller samples with 3×3 mm cross sections (these smaller samples were not used in calibration of power-law creep). DIC fields of axial strain (ε_{YY}) and in-plane rotation (ϕ) are shown. The distinct regions of in-plane rotation are noted. The in-plane shear fields are shown in Figure S7.

The grain sizes of the Na samples were approximately 1 mm, as shown in Figures S1 and S2. Because the grains are on the order of 1 mm in diameter, a cross-sectional slice of the 3×3 mm gauge section will contain only a few grains. Ideally, the tensile gauge section of a polycrystalline metallic sample would contain a sufficient number of grains in each cross-sectional slice to provide uniform deformation. However, in the case of these experiments, the relatively large grains in the small gauge section could result in local heterogeneity, as the deformation and rotation of each grain contributes a significant proportion of the cross-section's deformation.

The observed grain rotation in the samples with 3×3 mm cross sections suggests that grain size may be important for the viscoplastic behavior of Na in sodium-based batteries. For example, the grain size of electroplated metals will depend on a variety of factors, including current density, electrolyte composition, and substrate microstructure.[45] Therefore, depending on the relevant length scales, grain rotation effects may influence the local deformation behavior.

4 Discussion

4.1 Implications of creep in Na batteries

Since creep is activated in Na at unusually low stresses and low temperatures, the viscoplastic behavior of Na is expected to play a role in battery applications.

In Na metal batteries, electro-chemo-mechanical coupling is important to understand the relationships between between current density and strain rate. For example, as plating current density increases, compressive strains form as the anode volume expands against the surrounding solid materials. In our previous work on Li, a simplified, one-dimensional model was developed, which illustrated that power-law creep was the dominant deformation mechanism over the range of typical current densities for Li metal batteries (0.1 to 10 mA cm^{-2}), corresponding to strain rates in the range of 10^{-5} to 10^{-3} s^{-1}.[21] As shown in the present study, and consistent with previous reports,[26–28] power-law creep of Na is also the dominant deformation mechanism at room temperature over a wide range of strain rates. Therefore, it is important for future modeling efforts to incorporate the strain-rate and temperature-dependent deformation of Na when describing battery evolution.

In Na batteries with liquid electrolytes, the creep behavior of Na will influence how

dendrites form and interact with the separators within the battery. For example, local Joule heating at locations of current focusing could decrease the flow stress of Na. Furthermore, the local current density along the electrode electrolyte interface will vary as a result of spatially varying kinetics and the dynamic evolution of interface morphology,[46] which will subsequently modulate the local strain rate, and the corresponding flow stress of Na. These effects will be further amplified in 3-D electrode architectures, where current focusing and spatial heterogeneity can be distributed throughout the electrode volume.[47] Cumulatively, these effects can be thought of as positive or negative "feedback" mechanisms, where local mechanical phenomena can either amplify or suppress the evolution of features such as dendrites and pits.

In solid-state Na batteries, there are a number of important phenomena that relate to the temperature- and rate-dependent mechanical behavior of Na. Temperature-dependent creep will be enhanced at the global (cell) level when solid-state batteries are operated at elevated temperatures. As temperature increases, the ionic conductivity of Na-beta alumina increases according to an Arrhenius relationship.[48] As we show here, the power-law creep behavior of Na metal will also result in temperature dependence on the electrode side of the interface. These distinct temperature dependencies must be decoupled in order to fully understand the relationships between temeperature and performance. For example, it has been recently shown that a step increase in the critical current density (CCD) of Li metal SSBs can be observed across the melting temperature of Li.[49] This illustrates the importance of considering the physico-chemical properties of both sides of the interface (electrolyte and metal electrode) when describing the evolution of features such as voids and Li filaments.

In the event of Na filament penetration into the solid electrolyte, stress builds up and creates an interplay between viscous flow of the Na out of the crack, the ionic conductivity of the electrolyte, and the fracture toughness of the electrolyte, as predicted by modeling efforts.[50,51] Furthermore, during filament penetration, the effects of creep have been observed in the Li/LLZO system. Specifically, the filament tip was observed to retreat due to stress relaxation in Li and Li extrusion occurred at the free surface of the electrolyte.[52] It is expected that Na solid-state systems will have similar behavior, with a lower resistance to extrusion because of the low creep stress of Na. Such temperature-dependent flow of Na could be involved in the increase of critical current density (CCD) of Na-β''-alumina with respect to temperature.[48]

Finally, the unusually large grains that can be present in Na also factor into the mechanical behavior of Na metal foils and batteries. For example, during manufacturing, the crystallographic orientation dependence of bulk Na foil may translate into preferential deformation linked to specific grain orientations. At the microscale, there may also be effects from the crystallographic orientations of Na grains. For example, when Na is plated and forms in cracks in a solid-state electrolyte, certain grain orientations may exhibit more deformation. The rotational effects observed here from individual grains are also important to consider, which could affect deformation both during the initial manufacturing, as well as during plating and stripping. Our hope is that the experimental mechanics data presented here will facilitate future modeling efforts to deepen our understanding of grain-size and crystallographic orientation effects in Na metal batteries.

5 Conclusion

Tensile tests were performed on bulk samples of Na at various strain rates and temperatures. From stress-strain measurements between 273 and 348 K, the activation energy for power-law creep in Na was calibrated ($Q_c = 40 \pm 4$ kJ mol^{-1}). Also, through DIC measurements of the Na surface during deformation, significant grain rotation was observed, with up to about $\pm 3°$ of heterogeneous, local in-plane rotation for a set of samples with a relatively small cross-sectional area (9 mm^2). For larger samples (25 mm^2 cross-sections), local in-plane rotations were significantly smaller, and these larger samples were used for the power-law creep calibration. Furthermore, Levy-Mises flow was not observed from the in-plane DIC measurements. This was attributed to crystallographic anisotropy between the in-plane and through-thickness directions, with more deformation found in the through-plane direction. Together, these observations of power-law creep in Na will have an influence on Na-based battery applications with both liquid and solid electrolytes.

Acknowledgments

This material is based upon work supported by the National Science Foundation under grant No. 1751590. N.P.D. acknowledges support from the Scialog program sponsored jointly by Research Corporation for Science Advancement and the Alfred P. Sloan Foundation, including a grant from the Alfred P. Sloan Foundation. The authors are grateful to Ellen Arruda, Eric Kazyak, and Kuan-Hung Chen from University of

Michigan for insightful discussions. The authors also acknowledge the University of Michigan College of Engineering for financial support and the Michigan Center for Materials Characterization for use of the instruments and staff assistance.

References

[1] Manthiram A (2020) A reflection on lithium-ion battery cathode chemistry. Nature Communications 11(1):1–9, doi:10.1038/s41467-020-15355-0

[2] Olivetti EA, Ceder G, Gaustad GG, Fu X (2017) Lithium-Ion Battery Supply Chain Considerations: Analysis of Potential Bottlenecks in Critical Metals. Joule 1(2):229–243, doi:10.1016/j.joule.2017.08.019

[3] Chen L, Fiore M, Wang JE, Ruffo R, Kim DK, Longoni G (2018) Readiness Level of Sodium-Ion Battery Technology: A Materials Review. Advanced Sustainable Systems 2(3):1700153, doi:10.1002/adsu.201700153

[4] Taylor S, et al. (1964) Abundance of chemical elements in the continental crust: a new table. Geochimica et Cosmochimica Acta doi:10.1016/0016-7037(64)90129-2

[5] Vaalma C, Buchholz D, Weil M, Passerini S (2018) A cost and resource analysis of sodium-ion batteries. Nature Reviews Materials 3, doi:10.1038/natrevmats.2018.13

[6] Roberts S, Kendrick E (2018), The re-emergence of sodium ion batteries: Testing, processing, and manufacturability. doi:10.2147/NSA.S146365

[7] Pan H, Hu YS, Chen L (2013), Room-temperature stationary sodium-ion batteries for large-scale electric energy storage. doi:10.1039/c3ee40847g

[8] Yabuuchi N, Kubota K, Dahbi M, Komaba S (2014), Research development on sodium-ion batteries. doi:10.1021/cr500192f

[9] Bommier C, Ji X (2018) Electrolytes, SEI Formation, and Binders: A Review of Nonelectrode Factors for Sodium-Ion Battery Anodes. Small 14(16):1703576, doi:10.1002/smll.201703576

[10] Chen M, Liu Q, Wang SW, Wang E, Guo X, Chou SL (2019) High-abundance and low-cost metal-based cathode materials for sodium-ion batteries: problems, progress, and key technologies. Advanced Energy Materials 9(14):1803609, doi:10.1002/aenm.201803609

[11] Yadegari H, Sun X (2020) Sodium–Oxygen Batteries: Recent Developments and Remaining Challenges. Trends in Chemistry 2(3):241–253, doi:10.1016/j.trechm.2019.12.003

[12] Whitacre JF, Wiley T, Shanbhag S, Wenzhuo Y, Mohamed A, Chun SE, Weber E, Blackwood D, Lynch-Bell E, Gulakowski J, Smith C, Humphreys D (2012) An aqueous electrolyte, sodium ion functional, large format energy storage device for stationary applications. Journal of Power Sources 213:255–264, doi:10.1016/j.jpowsour.2012.04.018

[13] Kim H, Hong J, Park KY, Kim H, Kim SW, Kang K (2014) Aqueous Rechargeable Li and Na Ion Batteries. Chemical Reviews 114:11788–11827, doi:10.1021/cr500232y

[14] Famprikis T, Canepa P, Dawson JA, Islam MS, Masquelier C (2019) Fundamentals of inorganic solid-state electrolytes for batteries. Nature Materials doi:10.1038/s41563-019-0431-3

[15] De Jonghe LC, Feldman L, Buechele A (1981) Failure modes of Na-Beta alumina. Solid State Ionics 5:267–270, doi:10.1016/0167-2738(81)90244-7

[16] Ansell R (1986) The chemical and electrochemical stability of beta-alumina. Journal of Materials

Science 21(2):365–379, doi:10.1007/BF01145497

[17] Diederich ME, Trivisonno J (1966) Temperature dependence of the elastic constants of sodium. Journal of Physics and Chemistry of Solids 27(4):637–642, doi:10.1016/0022-3697(66)90214-9

[18] Fritsch G, Geipel F, Prasetyo A (1973) The elastic constants of sodium from 20 to 95°C. Journal of Physics and Chemistry of Solids 34(11):1961–1969, doi:10.1016/S0022-3697(73)80118-0

[19] Soma T, Kagaya S, Matsuo H (1981) Temperature Dependence of the Isothermal Elastic Constants of Alkali Metals. Physica Status Solidi (B) 106(1):309–314, doi:10.1002/pssb.2221060135

[20] McLellan RB, Angel YC (1996) The elastic behavior of sodium. Journal of Physics and Chemistry of Solids 57(11):1709–1711, doi:10.1016/0022-3697(96)00046-7

[21] LePage WS, Chen Y, Kazyak E, Chen KH, Sanchez AJ, Poli A, Arruda EM, Thouless MD, Dasgupta NP (2019) Lithium Mechanics: Roles of Strain Rate and Temperature and Implications for Lithium Metal Batteries. Journal of The Electrochemical Society 166(2):A89–A97, doi:10.1149/2.0221902jes

[22] Anand L, Narayan S (2019) An elastic-viscoplastic model for lithium. Journal of The Electrochemical Society 166(6):A1092, doi:10.1149/2.0861906jes

[23] Hull D, Rosenberg HM (1959) The deformation of lithium, sodium and potassium at low temperatures: Tensile and resistivity experiments. Philosophical Magazine 4(39):303–315, doi:10.1080/14786435908233342

[24] Herke P, Kirchner H, Schoeck G (1976) Plastic behaviour of sodium. In Conference proceedings of the International Conference on the Strength of Metals and Alloys, Nancy, France, 151–155

[25] Pichl W, Krystian M (1998) Plasticity and martensitic transformation of the alkali metals Li and Na. In Modelling of structure and mechanics of materials from microscale to product : proceedings of the 19th Risø International Symposium on Materials Science, vol. September, 429–434

[26] Sargent PM, Ashby MF (1984) Deformation mechanism maps for alkali metals. Scripta Metallurgica 18:145–150, doi:10.1016/0036-9748(84)90494-0

[27] Fincher CD, Zhang Y, Pharr GM, Pharr M (2020) Elastic and Plastic Characteristics of Sodium Metal. ACS Applied Energy Materials doi:10.1021/acsaem.9b02225

[28] Wang MJ, Chang JY, Wolfenstine JB, Sakamoto J (2020) Analysis of elastic, plastic, and creep properties of sodium metal and implications for solid-state batteries. Materialia 12:100792, doi:10.1016/j.mtla.2020.100792

[29] Fincher CD, Ojeda D, Zhang Y, Pharr GM, Pharr M (2020) Mechanical properties of metallic lithium: from nano to bulk scales. Acta Materialia 186:215–222, doi:10.1016/j.actamat.2019.12.036

[30] Xu C, Ahmad Z, Aryanfar A, Viswanathan V, Greer JR (2017) Enhanced strength and temperature dependence of mechanical properties of Li at small scales and its implications for Li metal anodes. Proceedings of the National Academy of Sciences of the United States of America 114(1):57–61, doi:10.1073/pnas.1615733114

[31] Herbert EG, Hackney SA, Thole V, Dudney NJ, Sudharshan Phani P (2018) Nanoindentation of high-purity vapor deposited lithium films: A mechanistic rationalization of the transition from diffusion to dislocation-mediated flow. Journal of Materials Research 33(10):1361–1368, doi:10.1557/jmr.2018.85

[32] Herbert EG, Hackney SA, Thole V, Dudney NJ, Sudharshan Phani P (2018) Nanoindentation of high-purity vapor deposited lithium films: A mechanistic rationalization of diffusion-mediated flow. Journal of Materials Research 33(10):1347–1360, doi:10.1557/jmr.2018.84

[33] Herbert EG, Dudney NJ, Rochow M, Thole V, Hackney SA (2019) On the mechanisms of stress relaxation and intensification at the lithium/solid-state electrolyte interface. Journal of Materials

Research 34(21):3593–3616, doi:10.1557/jmr.2019.313

[34] Liu Q, Zhang L, Sun H, Geng L, Li Y, Tang Y, Jia P, Wang Z, Dai Q, Shen T, et al. (2020) In Situ Observation of Sodium Dendrite Growth and Concurrent Mechanical Property Measurements Using an Environmental Transmission Electron Microscopy–Atomic Force Microscopy (ETEM-AFM) Platform. ACS Energy Letters 5(8):2546–2559, doi:10.1021/acsenergylett.0c01214

[35] Masias A, Felten N, Garcia-Mendez R, Wolfenstine J, Sakamoto J (2019) Elastic, plastic, and creep mechanical properties of lithium metal. Journal of materials science 54(3):2585–2600, doi:10.1007/s10853-018-2971-3

[36] Nachtrieb NH, Catalano E, Weil JA (1952) Self-Diffusion in Solid Sodium, part I. The Journal of Chemical Physics 20(8):1185–1188, doi:10.1063/1.1700708

[37] Nachtrieb NH, Weil JA, Catalano E, Lawson AW (1952) Self-diffusion in solid sodium, part II: the effect of pressure. The Journal of Chemical Physics 20(8):1189–1194, doi:10.1063/1.1700709

[38] LePage WS, Daly SH, Shaw JA (2016) Cross Polarization for Improved Digital Image Correlation. Experimental Mechanics 56:1–27, doi:10.1007/s11340-016-0129-2

[39] LePage WS, Shaw JA, Daly SH (2017) Optimum Paint Sequence for Speckle Patterns in Digital Image Correlation. Experimental Techniques doi:10.1007/s40799-017-0192-3

[40] Reu P (2014) All about speckles: aliasing. Experimental Techniques 38(5):1–3, doi:10.1111/ext.12111

[41] Barranger Y, Doumalin P, Dupré JC, Germaneau A (2012) Strain Measurement by Digital Image Correlation: Influence of Two Types of Speckle Patterns Made from Rigid or Deformable Marks. Strain 48(5):357–365, doi:10.1111/j.1475-1305.2011.00831.x

[42] Sedlatschek T, Lian J, Li W, Jiang M, Wierzbicki T, Bazant MZ, Zhu J (2021) Large-deformation plasticity and fracture behavior of pure lithium under various stress states. Acta Materialia 208:116730, doi:10.1016/j.actamat.2021.116730

[43] Sanchez AJ, Kazyak E, Chen Y, Lasso J, Dasgupta NP (2021) Lithium stripping: anisotropic evolution and faceting of pits revealed by operando 3-D microscopy. Journal of Materials Chemistry A doi:10.1039/D1TA03333F

[44] Mundy JN, Barr LW, Smith FA (1966) Sodium self-diffusion and the isotope effect. Philosophical Magazine 14(130):785–802, doi:10.1080/14786436608211972

[45] Sanchez AJ, Kazyak E, Chen Y, Chen KH, Pattison ER, Dasgupta NP (2020) Plan-view operando video microscopy of Li metal anodes: identifying the coupled relationships among nucleation, morphology, and reversibility. ACS Energy Letters 5(3):994–1004, doi:10.1021/acsenergylett.0c00215

[46] Wood KN, Kazyak E, Chadwick AF, Chen KH, Zhang JG, Thornton K, Dasgupta NP (2016) Dendrites and pits: Untangling the complex behavior of lithium metal anodes through operando video microscopy. ACS central science 2(11):790–801, doi:10.1021/acscentsci.6b00260

[47] Chen KH, Sanchez AJ, Kazyak E, Davis AL, Dasgupta NP (2019) Synergistic effect of 3D current collectors and ALD surface modification for high coulombic efficiency lithium metal anodes. Advanced Energy Materials 9(4):1802534, doi:10.1002/aenm.201802534

[48] Bay MC, Wang M, Grissa R, Heinz MV, Sakamoto J, Battaglia C (2020) Sodium Plating from Na-β''-Alumina Ceramics at Room Temperature, Paving the Way for Fast-Charging All-Solid-State Batteries. Advanced Energy Materials 10(3):1–8, doi:10.1002/aenm.201902899

[49] Kinzer B, Davis AL, Krauskopf T, Hartmann H, LePage WS, Kazyak E, Janek J, Dasgupta NP, Sakamoto J (2021) Operando analysis of the molten Li| LLZO interface: Understanding how the physical properties of Li affect the critical current density. Matter 4(6):1947–1961,

doi:10.1016/j.matt.2021.04.016

[50] Barroso-Luque L, Tu Q, Ceder G (2020) An analysis of solid-state electrodeposition-induced metal plastic flow and predictions of stress states in solid ionic conductor defects. Journal of The Electrochemical Society 167(2):020534, doi:10.1149/1945-7111/ab6c5b

[51] Shishvan S, Fleck N, McMeeking R, Deshpande V (2020) Growth rate of lithium filaments in ceramic electrolytes. Acta Materialia 196:444–455, doi:10.1016/j.actamat.2020.06.060

[52] Kazyak E, Garcia-Mendez R, LePage WS, Sharafi A, Davis AL, Sanchez AJ, Chen KH, Haslam C, Sakamoto J, Dasgupta NP (2020) Li Penetration in Ceramic Solid Electrolytes: Operando Microscopy Analysis of Morphology, Propagation, and Reversibility. Matter 2(4):1025–1048, doi:10.1016/j.matt.2020.02.008

[53] Messer R, Noack F (1975) Nuclear magnetic relaxation by self-diffusion in solid lithium: T1-frequency dependence. Applied Physics 6(1):79–88, doi:10.1007/BF00883553

[54] Pharr G, Ashby M (1983) On creep enhanced by a liquid phase. Acta metallurgica 31(1):129–138

Supplementary Information

Sodium mechanics: effects of temperature, strain rate, and grain rotation and implications for sodium metal batteries

William S. LePage[1,2], Yuxin Chen[1], Andrea Poli[1], M. D. Thouless[1,3], Neil P. Dasgupta[1,3,†]

[1] Department of Mechanical Engineering, University of Michigan, Ann Arbor, MI, 48109, USA

[2] Present address: Department of Mechanical Engineering, University of Tulsa, Tulsa, OK, 74104, USA

[3] Department of Materials Science and Engineering, University of Michigan, Ann Arbor, MI, 48109, USA

[†] Correspondence: ndasgupt@umich.edu

	Li	**Na**
Mass density (g/cc)	0.53	0.97
Melting point (°C)	180	98
Homologous temperature at 25°C	0.65	0.80
Standard reduction potential (V vs. SHE)	-3.04	-2.71
Abundance in Earth's crust[4]	0.0020%	2.4%
Activation energy for self-diffusion[36,37,53] (kJ mol^{-1})	50	43

Table S1: Comparison of selected properties of Li and Na.

	Temperatures	Mechanical testing methods	Strain measurements
Sargent and Ashby[26]	293 K	Bulk compression[54]	Grip displacement
Fincher et al.[27]	Room temp.	Nanoindentation, microhardness, and bulk compression	Indenter and grip displacement
Wang et al.[28]	Room temp.	Bulk pulse-echo, compression, and tension	Grip displacement
Present work	273 to 348 K	Bulk tension	Digital image correlation and grip displacement

Table S2: Experimental details from the present work and prior works on the viscoplasticity of Na.

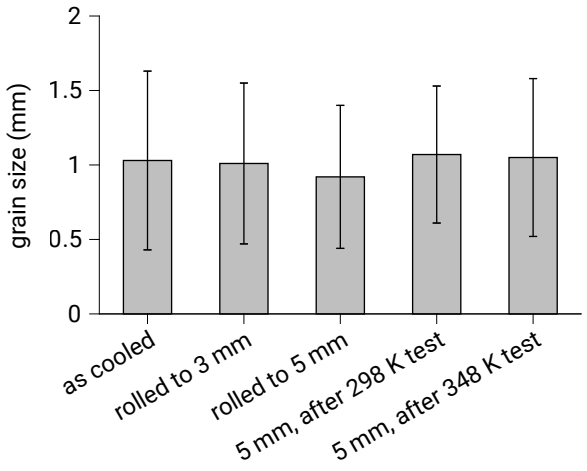

Figure S1: Grain sizes of the Na as measured from cross sections with an optical microscope before rolling (as cooled), after rolling to 3 mm and 5 mm, and after mechanical testing of the 5 mm-thick samples at 298 K and 348 K. The bar heights correspond to mean grain size, and the error bars indicate one standard deviation. At least 50 grains were measured for each sample.

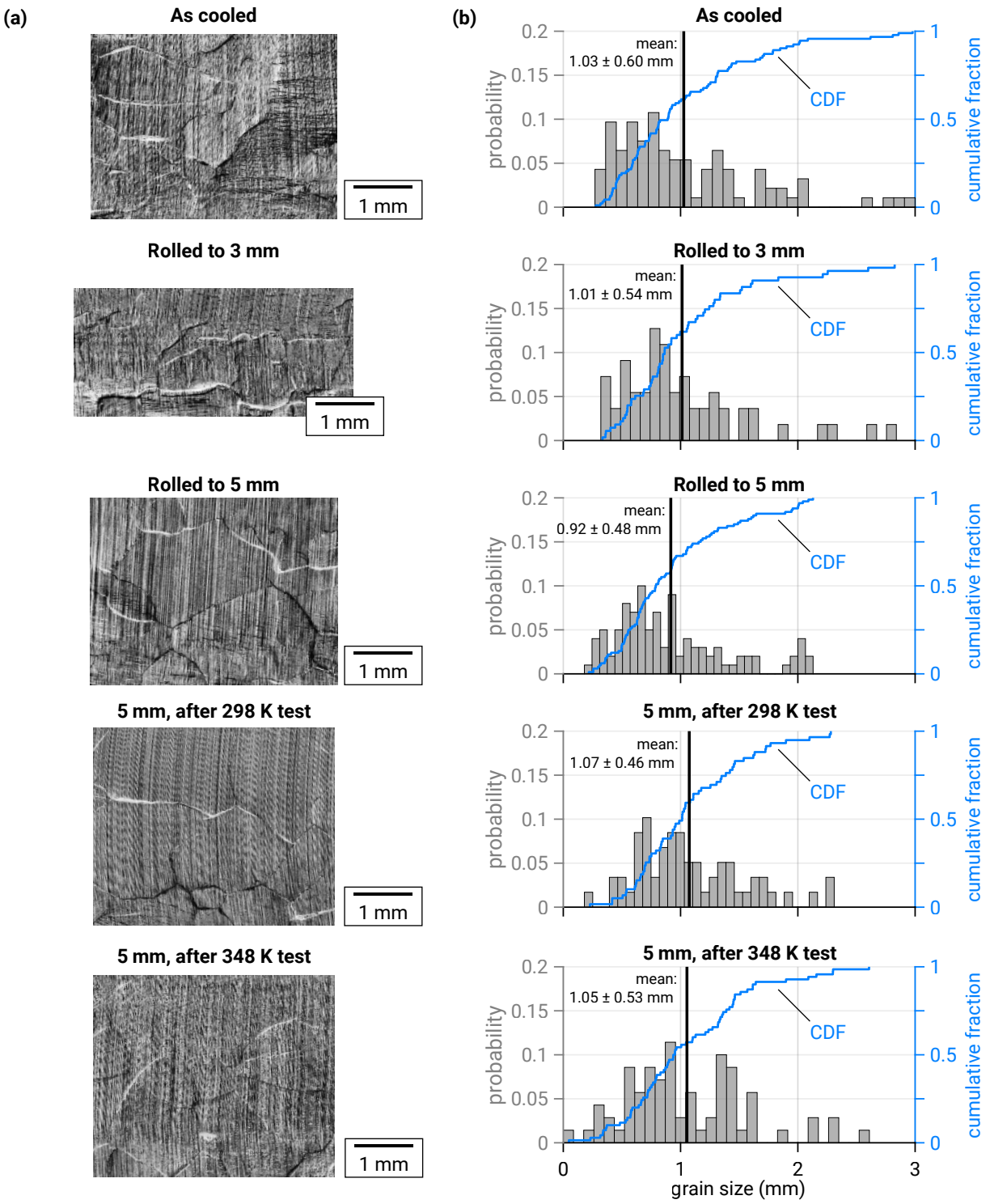

Figure S2: (a) Optical microscope images of cross sections for samples: as cooled (before rolling); after rolling to 3 mm and 5 mm; and after rolling to 5 mm and mechanical testing at 298 K and 348 K. (b) Probability distribution and cumulative distribution function (CDF) of grain sizes measured for the same sample conditions as (a). For each condition, at least 50 grains were measured.

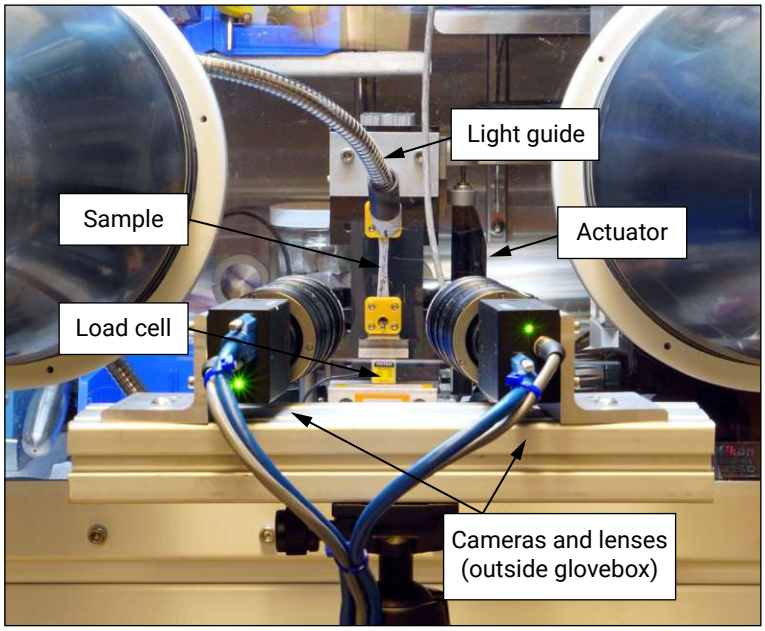

Figure S3: The glovebox-integrated mechanical testing system, with cameras and lenses mounted on a tripod outside the glovebox for DIC measurements.

Parameter	Value
Cameras	Flir GS3-U3-51S5M-C, 2448 × 2048 pixels
Lenses	Fujinon HF75SA-1, 75 mm focal length, f/16, with 10 mm of extension tubes
Illumination	Light source with two fiber-optic light guides (AmScope HL250-AY)
Field of view	32 × 38 mm (long axis of image positioned vertically)
Stereo-angle	15°
Standoff distances	51 cm
Image acquisition rate	Varied based on test displacement rate; up to 5 Hz
Patterning technique	212 to 250 μm black polyethylene microspheres (Cospheric) on base of MgO powder (Frey Scientific), for all samples used in power-law creep calibration; for the speckle pattern in the smaller set of samples with 3 × 3 mm cross-sections, graphite was used, following the procedure from prior work[21]
Approximate pattern feature size	0.5 mm (dark and bright features)
Software	Vic3D 7 (Correlated Solutions, Inc.)
Image filtering	Low-pass filter
Subset size	135 px, 2.1 mm
Step size,	10 px, 0.16 mm
Subset shape function	Affine
Strain formulation	Finite Lagrangian
Strain filtering	Gaussian window of 15 × 15 DIC data points
Maximum consistency threshold	0.02 px
Maximum confidence interval	0.05 px
Maximum matchability threshold	0.1 px

Table S3: Summary of the hardware and software parameters for digital image correlation (DIC) measurements.

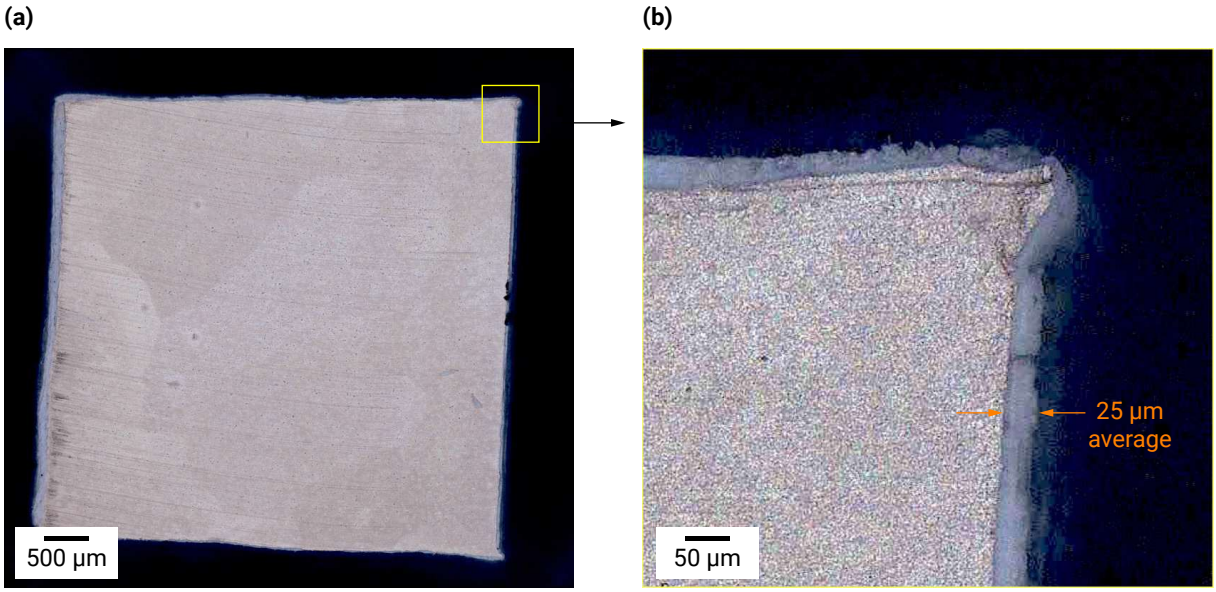

Figure S4: The oxidation layer was measured to be 25 µm thick after DMA testing with two air exposures (one air exposure < 60 s before mechanical testing, and one air exposure > 300 s after mechanical testing).

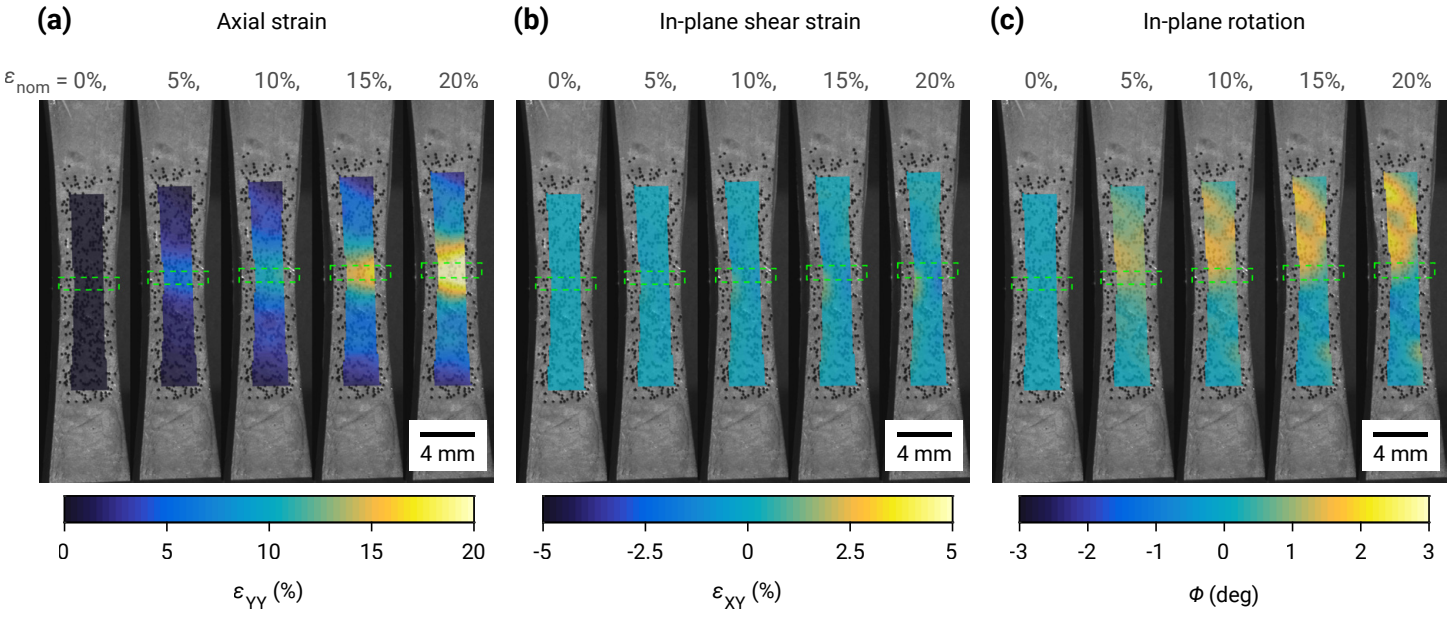

Figure S5: DIC fields of axial strain (ε_{YY}), in-plane shear strain (ε_{XY}), and in-plane rotation (ϕ) for a representative sample with 5×5 mm cross sections at 4×10^{-4} s^{-1} nominal strain rate. The selected area for ε_{nom} is shown in the central boxes with dashed lines.

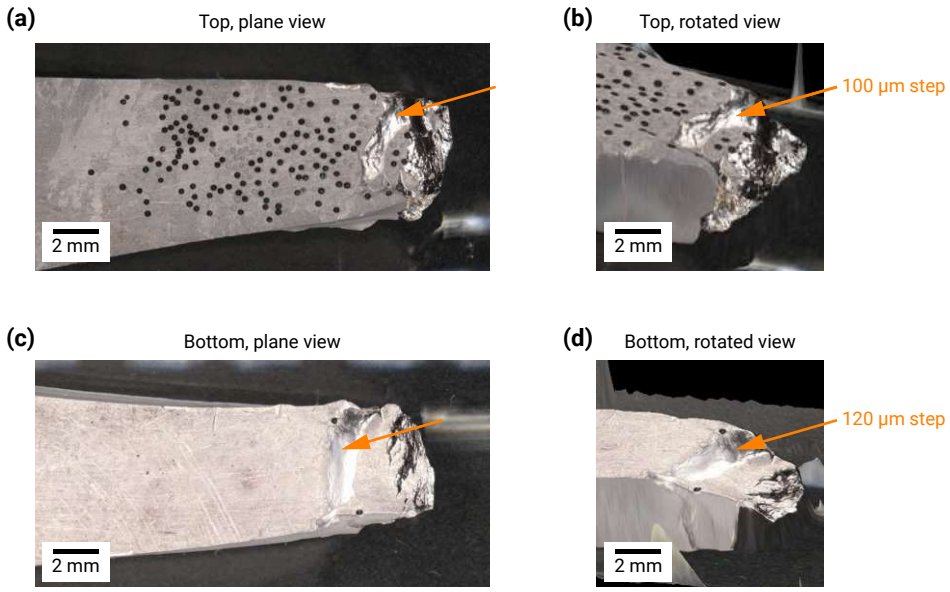

Figure S6: For a sample that was tested until ductile rupture, optical microscope images with calibrated, three-dimensional depth scanning (Keyence VHX-7000) revealed a 100 µm step change in the thickness for the top side of the same, and a 120 µm step change on the bottom.

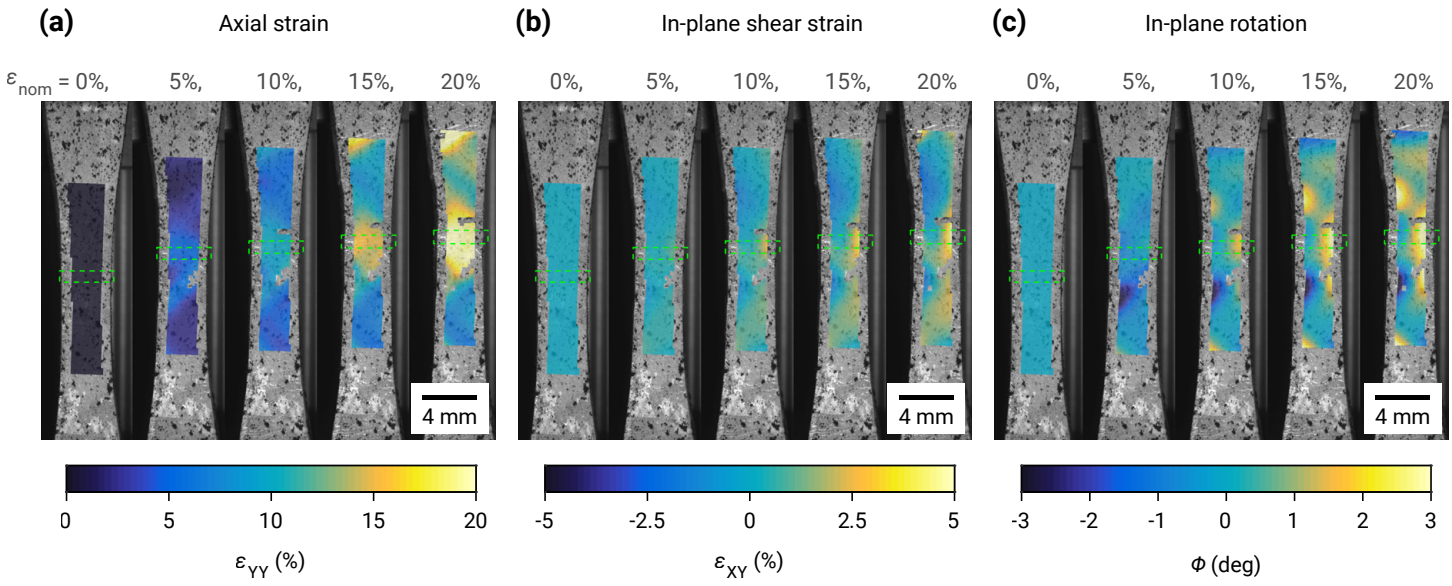

Figure S7: Grain rotation was prevalent for the smaller samples with 3×3 mm cross sections (these smaller samples were not used in calibration of power-law creep). DIC fields of axial strain (ε_{YY}), in-plane shear strain (ε_{XY}), and in-plane rotation (ϕ) are shown. The distinct regions of in-plane rotation are noted.

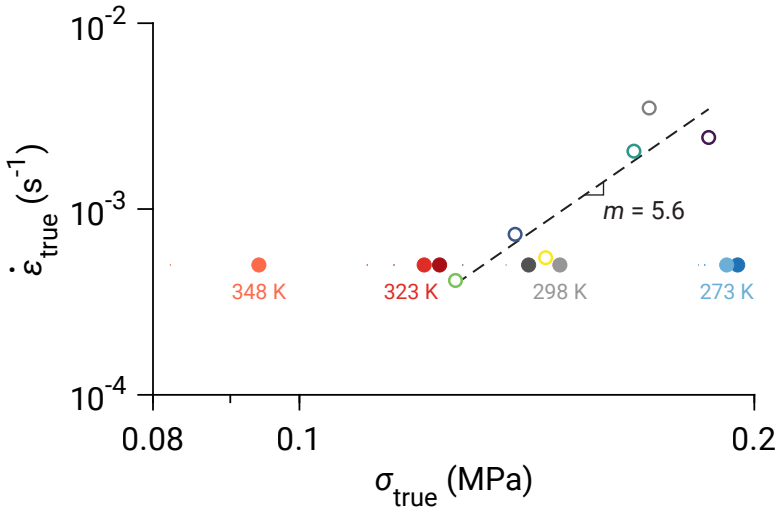

Figure S8: For the average values of true stress and true strain rate, the measurements from DIC (open circles) were consistent with the measurements from DMA (closed circles).

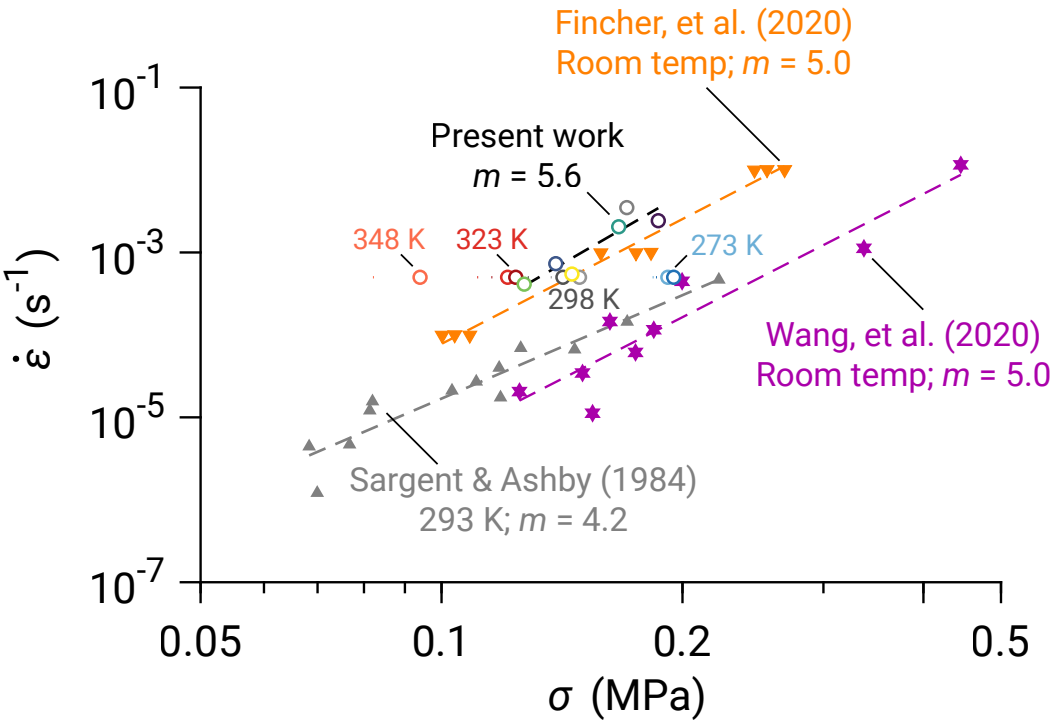

Figure S9: Fits of the power-law exponent m from the present work (open circles), Sargent and Ashby (gray triangles),[26] Fincher et al. (orange inverted triangles),[27], and Wang et al. (purple stars).[28] Note that the values from the present work are fitted with the true stress and true strain rate values, while the other works match their published values, stated as nominal stress and strain rate in Wang et al. and assumed to be the nominal values for Sargent and Ashby and Fincher et al.